VECTORED THRUST EVTOL FLIGHT DYNAMICS MODELING AND REAL-TIME SIMULATION

Liangjun Li[a] Fan Sun[a] Yiran Gong[a] Tianheng Yao[a] Wei Zhang[a,b] Chen Jiang[a,*] Haowen Wang[a]

[a] School of Aerospace Engineering, Tsinghua University, Beijing 100084, China

[b] Zhuhai Lonhua Helicopters Technology Co., Ltd., Zhuhai 519070, Guangdong, China

Abstract

Vectored thrust eVTOL is one of the important development directions for future rotorcraft. With the diverse configuration and complex aerodynamic interference, it is difficult for the traditional modelling method to simultaneously achieve the requirements of flexible modelling, high fidelity and real-time simulation. In this paper, a component-based method for real-time simulation of vectored thrust eVTOL and an aerodynamic interference model based on slipstream theory and viscous vortex particle correction are proposed. These methods are used to establish a flight dynamics model of a vectored thrust eVTOL aircraft. The model underwent flight simulation on a hardware-in-the-loop simulation platform. The results show that the modeling method is capable of simulating the tilt transition phase; the aerodynamic interference will reduce the frequency and damping of the longitudinal short-period modes of the whole aircraft at the end of the tilt transition phase and the low-speed flight phase of the fixed-wing mode.

1. NOTATION

Symbols

C_D	Drag Coefficient
C_L	Lift Coefficient
C_P	Power Coefficient
C_T	Thrust Coefficient
FM	Figure of Merit
J	Advance Ratio of Propeller
k_d	Axial Velocity Development Factor
R_0	Semi-expanded Thickness of Termination Surface of Zone of Contraction
R_d	Semi-expanded Thickness of Termination Surface of Zone of Flow Establishment
R_h	Radius of Hub
R_p	Radius of Propeller
V_∞	Free Stream Velocity
x_0	Length of Zone of Contraction
x_d	Length of Zone of Flow Establishment
α	Angle of Attack
α_s	Rotor shaft Angle of Attack
β	Pitch Angle of Propeller
δ_{lon}	Longitudinal Control
μ	Advance Ratio

Acronyms:

AOA	Angle of Attack
ATB	Advanced Technology Blade
CFD	Computational Fluid Dynamics
eVTOL	electric Vertical Take-off and Landing
ODE	Ordinary Differential Equation
RAE	Royal Aircraft Establishment
ROBIN	Rotor Body Interaction
VFS	Vertical Flight Society
VLM	Vortex Lattice Method
VPM	Vortex Particle Method
ZEF	Zone of Established Flow
ZFE	Zone of Flow Establishment

* Corresponding Author.

2. INTRODUCTION

The relentless growth of urban populations, unaccompanied by strategic transportation infrastructure planning, has necessitated individuals to endure prolonged hours commuting between their residences and workplaces. This unwelcome reality has far-reaching consequences, adversely impacting not only the physiological wellbeing of commuters but also the environment and the economy (Ref. 1).

Urban Air Mobility (UAM) holds immense potential in mitigating traffic congestion and environmental pollution prevalent in densely populated urban areas. The pivotal enabler for the realization of UAM lies in electric Vertical Take-Off and Landing (eVTOL) aircraft. Thanks to the maturity of batteries, motors and electronic control technology, as well as the inherent attributes of electric drive technology such as rapid response, extensive speed range, and minimal noise emissions, eVTOLs offer a significantly more adaptable configuration (Ref. 2).

Specifically, eVTOLs are categorized into five configurations (Ref. 3). Among them, the vectored thrust eVTOL incorporates rotors that can be fully or partially tilted, effectively amalgamating the advantages of a distributed layout and tilting rotor characteristics. This configuration offers significant benefits in terms of speed and range (Ref. 4); however, it also presents numerous novel challenges in design, simulation, control, and other related aspects.

Real-time simulation plays a crucial role in the development of eVTOL models, airworthiness certification, and operator training (Ref. 5). To ensure its effectiveness in simulating the tilt process, real-time simulation necessitates flight dynamics models with computational speed meeting real-time requirements and possessing high confidence levels (Ref. 6).

The research emphasis for rotorcraft real-time flight dynamics simulation models typically revolves around enhancing the model's fidelity (Ref. 7-8). Due to differences in configuration and other aspects, the modeling methods for rotorcraft flight dynamics are not fully compatible with the modeling requirements of eVTOL. Specifically, two key aspects need to be addressed: firstly, the flexibility of configurations necessitates an approach that can seamlessly integrate component models into a comprehensive aircraft model without any limitations on the model configuration; secondly, the intricate nature of aerodynamic interference renders it arduous to rely solely on empirical models and correction coefficients for aerodynamic interference modeling.

In recent years, there has been significant progress in the flight dynamic modeling of vectored thrust eVTOL. Cook (Ref. 9) has established a model of tiltwing based on the slipstream theory. Simmons (Ref. 10) developed tiltwing mathematical models from experimental data. However, tiltwing is a special configuration of vectored thrust eVTOL. It only needs to consider the aerodynamic interference of the propeller-wing, without involving the aerodynamic interference of rotor-wing. The aforementioned two studies cannot be extended to other configurations. Gladfelter (Ref. 11) successfully established a real-time simulation model for tiltwing eVTOL using ART's FLIGHTLAB software. The aerodynamic interference was calculated using the viscous vortex particle method to obtain the correction coefficient. This study only calculated the trim results for the tilt process and did not conduct simulations.

Furthermore, Prabhakar (Ref. 12) developed linear models for both multi-rotor and fixed-wing modes of vectored thrust eVTOL and performed flight simulations; nevertheless, they did not address the simulation of the aircraft's tilt transition process. Stoll (Ref. 13-14) integrated the CFD method and surrogate model method to derive the propeller model and establish a model for vectored thrust eVTOL. While this model adequately addresses balance analysis in tilt transition strategies, it is not suitable for dynamic simulations. Wang (Ref. 15) based on transient CFD established a dynamic model of a tilt-rotor unmanned aerial vehicle and conducted simulations specifically targeting the tilt transition phase. However, this study does not fully simulate the tilt transition phase and does not discuss real-time performance.

Although CFD-based methods or experiment-based approach can build model relatively easily and take aerodynamic interactions into account, significant time is required for re-computation when the configuration is adjusted. In the early and middle stages of product development, it is more necessary to use some configuration-independent modeling methods.

In summary, the existing research is deficient in two aspects: firstly, there is a paucity of studies that real-time simulate the tilt transition phase, and secondly, a configuration-independent aerodynamic interference model for vectored thrust eVTOL.

In this paper, a modeling method that considers rotor/propeller-wing aerodynamic interference for real-time simulation of vectored thrust eVTOL is proposed. The foundation of modeling method lies in the work by Fan Sun (Ref. 16).

The paper encompasses three main components:

1. A modeling method for real-time simulation of vectored thrust eVTOL.

2. A rotor/ propeller-wing aerodynamic interference model for real-time simulation.

3. Flight dynamics simulation of the vectored thrust eVTOL and analyze the impact of the aerodynamic interferences.

3. COMPONENT MODELING AND VALIDATION

The eVTOL configurations featuring vectored thrust exhibit significant diversity, where the entire aircraft is an integrated assembly of rotors, wings, fuselage, and other components. This paper utilizes a component-based approach for dynamic modeling of eVTOL. The models of individual components are independent of the configuration, which enables this methodology to be rapidly applied to different eV-TOL configurations, including diverse rotor parameters, numbers and placement of rotors, as well as wing sizes and placement. Consequently, the flight dynamics model of the eVTOL aircraft can be synthesized by aggregating the models of its constituent parts. Given the scarcity of experimental data specifically for vectored thrust eVTOLs, the validation of the modeling methodology is confined to the verification of the primary component models, thereby demonstrating the effectiveness of the pro-posed approach.

3.1. Rotor/ Propeller Model

The rotors utilized in eVTOLs are often designed with smaller dimensions and higher solidity, leading to negligible elastic deformations in their blades. Consequently, this study adopts a rigid blade assumption, which simplifies the modelling process. Notably, both the rotors and propellers are modelled using an identical approach, with each blade modelled individually. To ensure accurate representation of the blade's kinematic behavior, flap hinge, lag hinge, and pitch hinge are strategically placed between the hub and each blade, as illustrated in Figure 1. This configuration captures the essential dynamics of the rotor system, facilitating accurate predictions and simulations.

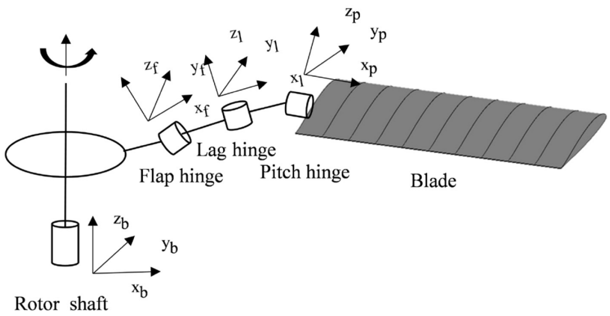

Figure 1: Schematic diagram of Single-Blade Structures in Rotor Systems

In flight dynamics simulation, dynamic inflow is used to calculate the induced velocity distribution of rotor disk. Furthermore, based on the blade element theory, a two-dimensional airfoil aerodynamic database is utilized to compute the aerodynamic forces acting on each blade element. This methodology ensures that each blade is treated independently, with its own set of aerodynamic forces calculated based on its specific position and orientation within the rotor system.

The VPM (Ref. 17), despite its high fidelity in simulating rotor flow fields, is hindered by its slow computational speed, making it impractical for direct application in real-time simulations. Therefore, the VPM is utilized to calculate the induced velocities on the rotor disk plane, as well as the aerodynamic interference velocities at the control points. The outcomes of the VPM calculations will subsequently be utilized to fit and refine the aerodynamic interference model proposed in the subsequent sections

3.2. Wing Model

In this study, the wings are modelled as rigid bodies. The aerodynamic forces acting on the wings are computed using VLM (Ref. 18), which is illustrated in Figure 2. To account for the influence of control surface deflection, vortex lattices are strategically placed on the control surfaces, enabling the model to capture the effects of these deflections on overall aerodynamic performance. To further enhance computational efficiency, the study pre-computes the influence coefficient matrices and their inverses for various control surface deflection angles.

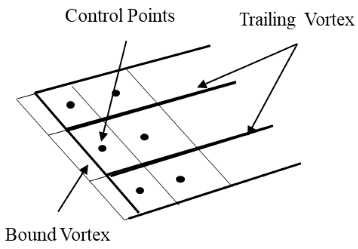

Figure 2: Schematic diagram of VLM

3.3. Other Components Model

The fuselage is modeled as a six-degree-of-freedom rigid body, neglecting aerodynamic interactions between the fuselage and other components for simplicity and computational efficiency. The aerodynamic forces and moments acting on the fuselage are determined either through CFD simulations, or by utilizing experimental data obtained from wind tunnel tests.

The tilting mechanism of the eVTOL aircraft is modelled as a combination of a revolute joint and a prismatic joint, disregarding elastic effects for simplicity and computational efficiency.

3.4. Rotor/ Propeller Model Validation

In this paper, the validity of rotor/Propeller modelling is verified respectively using an Advanced Technology Blade (ATB) developed by Bell and a small propeller test by Deters at the University of Illinois.

The ATB rotor tests were conducted in 1984 at NASA Ames Research Centre (Ref. 19). In this paper, we compare Power Coefficient and Figure of Merit at different Thrust Coefficient and the results are shown in Figure 3.

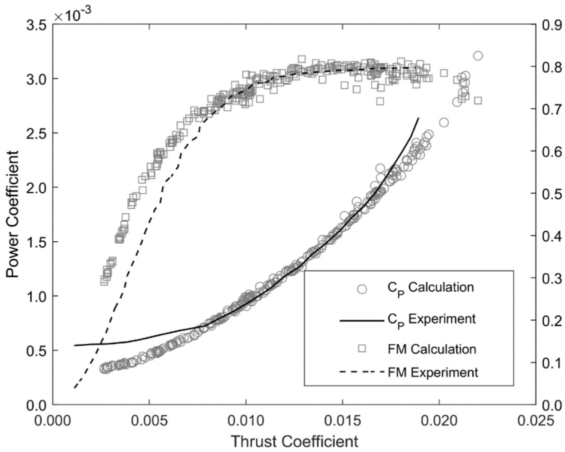

Figure 3: Variation of Power Coefficient (C_P) and Figure of Merit (FM) with Thrust Coefficient (C_T)

The calculation results are in good agreement with the test values in the range of medium Thrust Coefficient. In the case of lower C_T, FM calculated by this model is lower andC_T is high; in the case of higher C_T, C_P calculated by this model is higher. To analyze the reasons for the inaccuracies, the estimation of the profile power in the case of lower C_T is relatively larger, resulting in an over-estimation of the total power and the proportion of ideal induced power is under-estimated. In contrast, under conditions of higher thrust coefficient, induced power is over-estimated.

This paper uses the GWS 5x4.3 isolated propeller test case conducted by Deters (Ref. 20) for verification. The comparison results are shown in Figure 4-Figure 5.

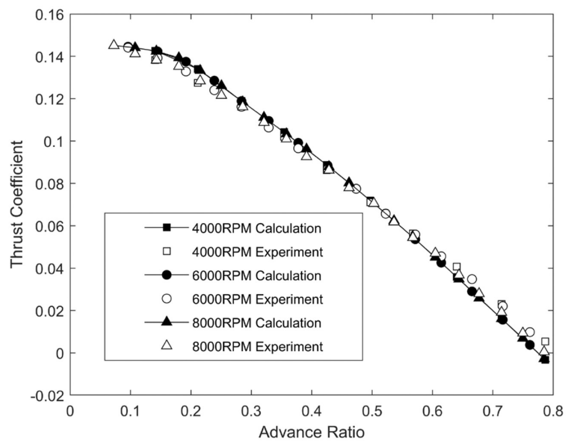

Figure 4: Variation of GWS Propeller's C_T with Advance Ratio

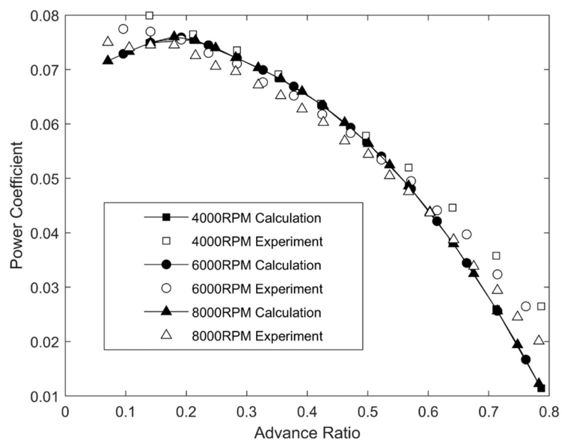

Figure 5: Variation of GWS Propeller's C_P with Advance Ratio

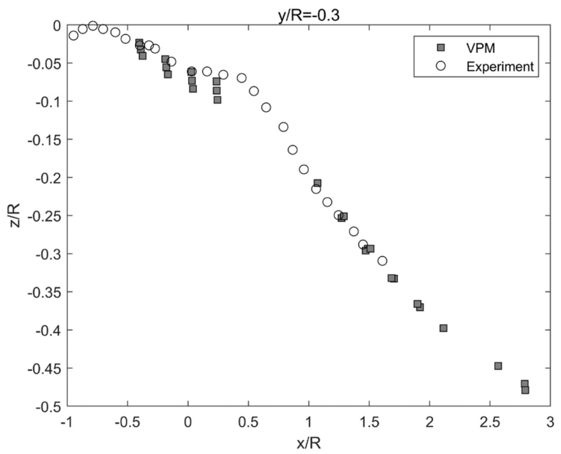

Figure 6: Distribution of Blade-tip Vortices in $y/R = -0.3$ cross-section ($\mu = 0.15$)

VPM is verified by ROBIN rotor wake experiment (Ref. 21). In this experiment, 2MRTS (2-Meter Rotor Test System), which is a set of scaled rotor, is adopted (Ref. 22). The rotor's thrust coefficient is $C_T = 0.0064$. In order to verify the effectiveness of VPM, the distribution of blade-tip vortices in XZ cross-sections is calculated and compared with the experiment, as is shown in Figure 6.

It can be observed that VPM used in this paper captures the distribution of blade-tip vortices effectively.

3.5. Wing Model Validation

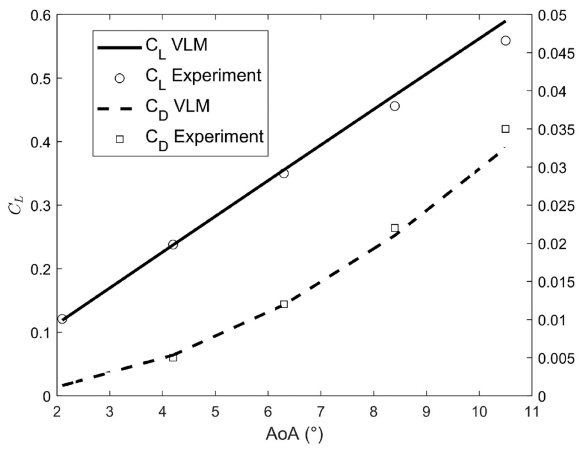

Figure 7: Comparison of Wings' Lift Coefficient at different AOA

This paper employs the wind tunnel experiment on a wing conducted by Weber from the Royal Aircraft Establishment (RAE) in 1949 (Ref. 23) for wing verification. The wing used in the experiment had a span of 2.489 meters, a chord length of 0.508 meters, a sweep angle of 45°, and the airfoil was a symmetrical RAE101. The calculation in this section uses 80 vortex lattices, with 40 uniformly distributed in the spanwise direction and two rows in the chordwise direction. The calculation results are shown in Figure 7 and Figure 8.

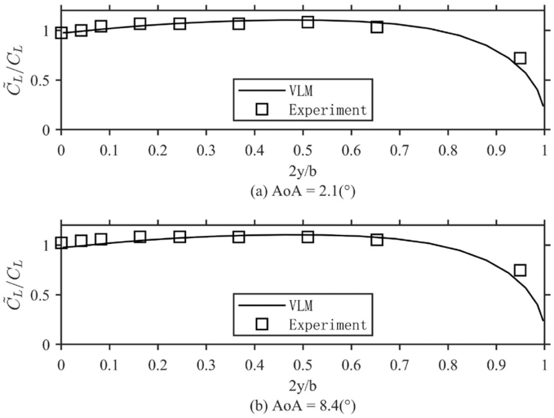

Figure 8: Comparison of Wings' Lift Coefficient Distribution

It can be observed that VLM used in this paper accurately calculates the lift coefficient of the wing and its distribution along the span at different AOA.

4. AERODYNAMIC INTERFERENCE MODELLING AND VALIDATION

Considering the small influence of the downstream wing on the upstream propeller (Ref. 24), the aerodynamic interference model only calculates the aerodynamic interference of the upstream propeller on the downstream wing and the downstream propeller. The specific method is to calculate the axial and tangential velocity distributions of the flow field downstream of the propeller based on the time-averaged assumption, and superimpose the velocity field at the control point of the downstream wing/propeller.

4.1. Propeller Slipstream Model

The slipstream of the propeller is accelerated and contracted in the near field driven by the pressure of the propeller. in the far field by the viscous and turbulent flow, it starts to expand until the velocity is equal to the ambient flow. The flow field model downstream of the propeller is mainly a three-region model (Ref. 25-26), including the zone of contraction, the zone of flow establishment (ZFE) and the zone of established flow (ZEF).

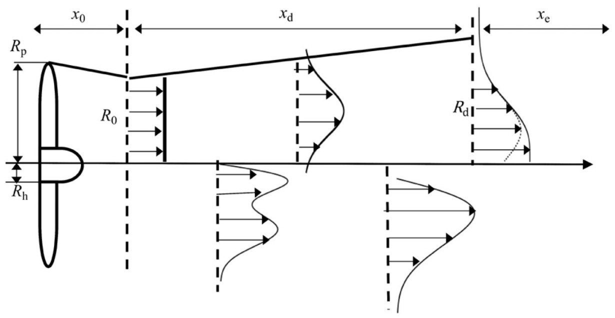

Figure 9: Distribution of Propeller's Wake Velocity

In this paper, improvements are made in the form of axial and tangential velocity distributions in ZFE; and the scope of application of the velocity self-similarity law, with the following assumptions:

1. The axial velocity distribution in ZFE gradually merges from a bimodal distribution to a unimodal distribution as the axial position increases, and the merged position is the end position of ZFE.

2. The distribution of tangential velocity in ZFE is characterized by two centrally symmetrical peaks, the first near the blade root and the second peak occurring near the blade tip.

3. The distribution of axial and tangential velocities follows the self-similarity law in ZFE and ZEF.

Based on such assumptions, the velocity distributions in the three regions are shown in Figure 9.

As is shown in Figure 9, R_p is Radius of the Propeller, and R_h is Radius of the Hub. In the zone of contraction, the case of no viscous contraction of the airflow is mainly considered, in which the airflow is accelerated and the flow field is contracted. The length of the zone of contraction is x_0, and the semi-expanded thickness of the termination surface of the zone of contraction is R_0. The length of ZFE is represented by x_d, and the semi-expanded thickness of the termination surface is R_d, when the two peaks of the axial direction are merged. The velocity distribution and wake radius in ZEF develop downstream according to the law of conservation of axial and angular momentum.

The zone of contraction is modelled based on the Stone (Ref. 27) method for velocity distribution. Neglecting viscous effects and assuming the slipstream as a series of flow tubes, the slipstream is calculated from inside out, and based on the conservation of mass and angular momentum in the flow tubes, the axial velocity u, tangential velocity w are acquired.

(1) $$u_s = k_d u_0$$

(2) $$w_s = w_0 \exp\left[-\left(\frac{r}{d}\right)^2\right]$$

The subscript s indicates the downstream axial position x_s, and k_d is the axial velocity development factor. $u_{0,m}, w_{0,m}, d$ are the initial value that needs to be input.

In ZFE, the assumption of the self-similarity law is adopted, which means that velocity takes the same form at different locations.

The decay of axial velocity is considered linear, while tangential velocity is considered to decay exponentially. Therefore, the axial direction of ZFE downstream of the propeller is shown below:

(3) $$u = u_\infty + \left(1 - c_1 \frac{x}{x_d}\right) u_0 \left(e^{-\frac{(r-r_u)^2}{b^2}} + e^{-\frac{(r+r_u)^2}{b^2}}\right)$$

The axial velocity is represented by two Gaussian distributions symmetrical about the hub, which are used to model the effect of the hub. r_u denotes the distance between the two peaks, and b denotes the semi-extended thickness of the jet flow. c_1 is the attenuation factor of the axial velocity. Near the zone of contraction, b is smaller. And because of r_u, two Gaussian distributions have lower velocity at the axis of rotation. As b increases, velocity of the two Gaussian distributions is superimposed at the axis of rotation and gradually merge into one peak of velocity.

The distribution of tangential velocity is shown below:

(4) $$w = w_0 e^{-c_2\left(\frac{x}{x_d}\right)} \left(\frac{r}{kb} e^{1-\left(\frac{r}{kb}\right)^2} + e^{-\left(\frac{r-r_w}{kb}\right)^2} - e^{-\left(\frac{r+r_w}{kb}\right)^2}\right)$$

w_0 is the maximum time-averaged velocity of the Gaussian distribution at the initial position of ZFE. c_2 is the tangential velocity decay factor, and k is the difference coefficient between the tangential and axial velocity spreading.

The tangential velocity is divided into three parts in order to ensure that the velocity distribution is centrosymmetric about the hub center, i.e., the first part of the equation adopts the centrosymmetric velocity distribution with the peak close to the hub, which is used to represent the first peak of the tangential velocity, and the other peak is described by the Gaussian distribution with two centrosymmetric distributions. Similar to that of the axial velocity distribution, r_w represents the distance between the two peaks.

ZFE is modelled as the main section of an unpressurised axisymmetric rotating jet flow considering the external flow, with axial flux conservation of axial and angular momentum (Ref. 28). Self-similarity assumptions are made on the axial and tangential velocity of the rotating jet flow in terms of section distribution based on experimental data.

Estimated below is variation along the axial direction of u_m and w_m according to the exponential relationship.

(5) $$u_m \propto x^p, b \propto x^q, w_m \propto x^s$$

Considering the induced velocity of the propeller $w_m < u_m$, the attenuation of the tangential velocity is generally greater than the axial velocity. It can hereby be deduced that

(6) $$\frac{d}{dx}\left\{\left[F_0\left(\frac{u_\infty}{u_m}\right)+F_1\right]b^2u_m^2\right\}=0$$

F_0 and F_1 are constants calculated from the self-similarity law.

For strong jet flow, $u_m/u_\infty \gg 1$, using a similar relationship, combined with the above derivation yields:

(7) $$b \propto x$$

Combined with the test data of the propeller (Ref. 29), the expansion relationship of the propeller in ZEF can be written as:

(8) $$b = 0.2241(x - x_d)$$

In ZEF, the maximum value of axial velocity and the maximum value of tangential velocity at any position are obtained, and then the axial and tangential velocity distributions are solved for the given axial and radial positions.

4.2. Validation of Propeller-Wing Aerodynamic Interference

In this paper, tests on wind tunnel model PROWIN (Ref. 30) are used to verify propeller-wing aerodynamic interference. The subject in the PROWIN wind tunnel model consisted of a straight wing with no twist and a propeller installed on the wing.

Results of calculation are listed below. Figure 10(a) shows that the wing model used in this paper is able to accurately compute the lift when the propeller is turned-off, i.e., when aerodynamic interference is not considered. Figure 10(b) shows that the lift of the wing is also accurately calculated when the propeller is turned-on, i.e., considering aerodynamic disturbances. In addition, the model is able to accurately predict the effect of different rotational directions of the propeller on the wing lift coefficient, and the inboard upward rotating propeller will slightly increase the lift of the wing compared to the outboard upward rotating propeller. For a 10° angle of attack (AOA) of the wing, the inboard upward propeller increases the wing lift by about 15% and the outboard upward propeller increases the wing lift by about 11%.

The lift distribution of the wing at 0° and 4° AOA is given in Figure 11.It can be found that at different AOA, the aerodynamic interference model used in this paper can reflect the main effect of propeller-wing interference: the lift of the wing part behind the upward propeller increases, and the opposite for the downward propeller.

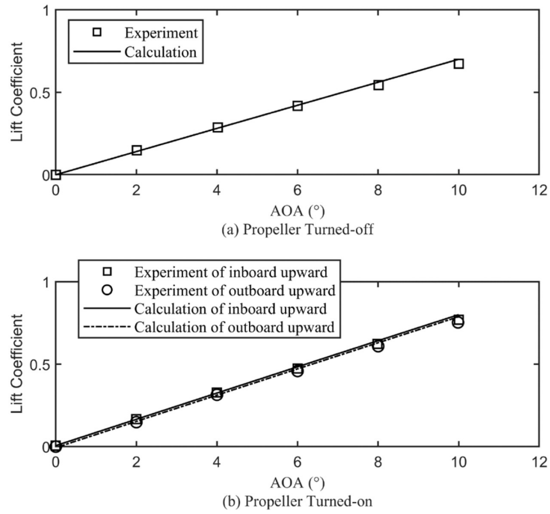

Figure 10: Curve of Wing's Lift Coefficient

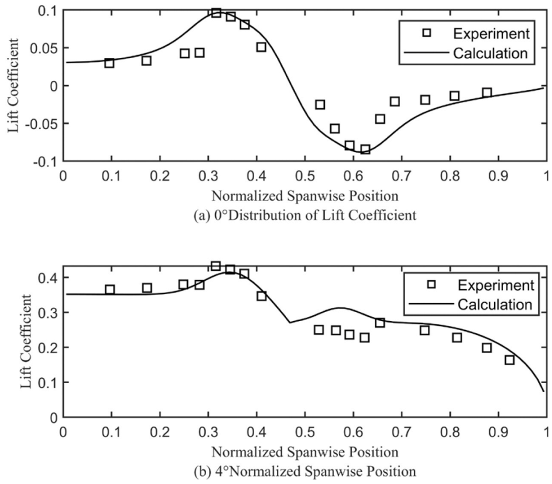

Figure 11: Distributions of Wing's Lift Coefficient

4.3. Validation of Propeller-Propeller Aerodynamic Interference

In this paper, the wind tunnel test at Delft University (Ref. 31) is used to verify the aerodynamic interference of propeller-propeller. The propeller used in the wind tunnel experiment at Delft University originated from the Fokker's F29 project, and this paper denotes the propeller by F29. The two propellers are a pusher propeller and a tractor propeller, placed as shown in Figure 12.

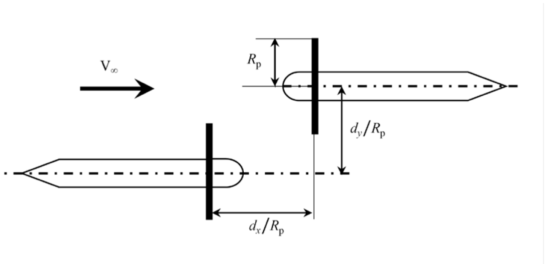

Figure 12: Schematic diagram of Wind Tunnel Test of F29

In the experiment, the radius of propellers is $R_p = 0.1524m$, and free stream speed is $V_\infty = 20m/s$. d_x, d_y shows the relative position of the two propellers.

Firstly, the isolated rotor model of F29 is built for performance calculation using the rotor modelling method in this paper, and Figure 13 shows the calculation results. The results show that the rotor model in this paper can effectively calculate the thrust coefficient and power coefficient of F29.

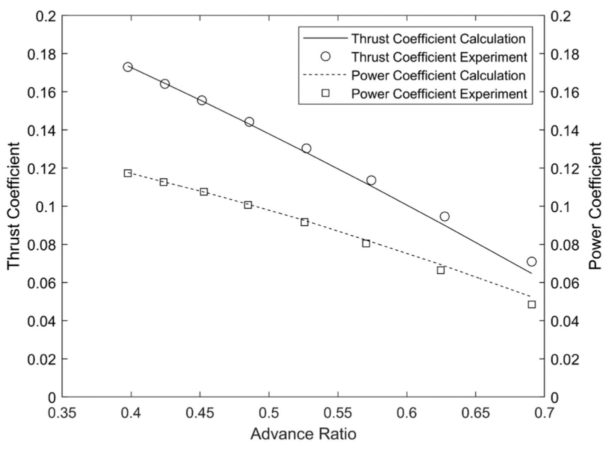

Figure 13: Verification of Results of F29 Calculation

Aerodynamic interference is subsequently considered. The propeller slipstream model proposed in this paper is used to calculate the axial and tangential velocity field downstream of the propeller. And then the influence of the front propeller on the rear propeller at advance ratio of 0.49 and 0.57, $d_x/R_p = 0.6$, $d_x/R_p = 5.5$ is calculated. The ratio of the thrust coefficient C_{TOAA} and power coefficient C_{POAA} of the rear propeller to the thrust coefficient C_{TISO} and power coefficient C_{PISO} of the isolated propeller is compared, and the results are shown in Figure 14-Figure 15.

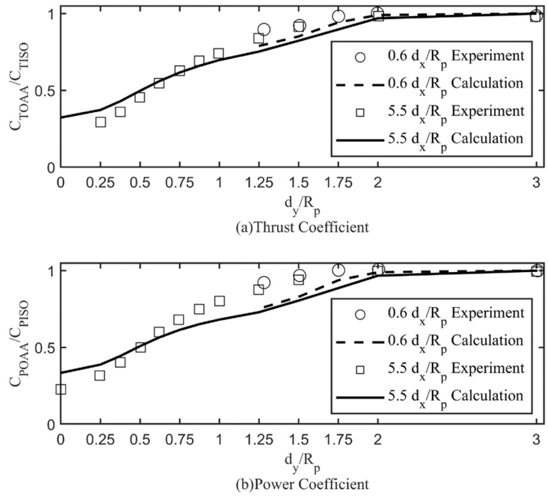

Figure 14: Variation of C_T 、 C_P with y/R_p at Advance Ratio of 0.49

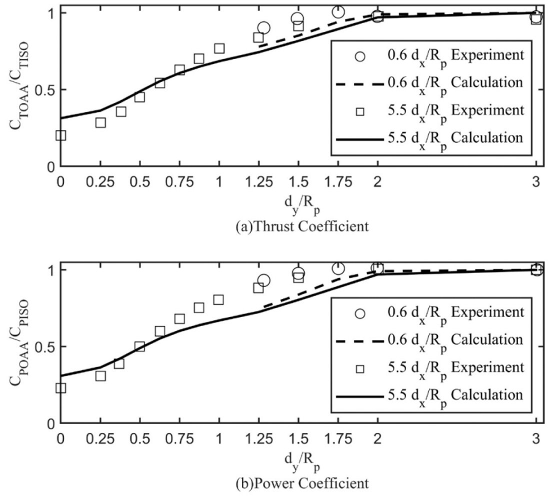

Figure 15: Variation of C_T 、 C_P with y/R_p at Advance Ratio of 0.57

Comparison of results shows that the front propeller will have unfavorable effects on the tractor force and power of the rear propeller. As the overlap of the two propellers decreases, the effect of the front propeller on the rear propeller gradually decreases. At $d_y/R_p = 2$, the effect of the front propeller on the rear propeller can be neglected. Comparing the effects of $d_x/R_p = 0.6$ and $d_x/R_p = 5.5$, it can be found that the effect of the front propeller on the rear propeller is slightly higher in the farther position than in the near position. The tractor force and power of the two propellers under different advance ratios will be different, and the influence of aerodynamic interference is similar.

4.4. Rotor-Wing Aerodynamic Interference

During low-speed and tilt transition phase of vectored thrust eVTOL, the rotor is in oblique flow. The aerodynamic interference model based on the slipstream theory exhibits significant errors when calculating rotor-wing aerodynamic interactions. In this paper, the VPM is employed to calculate the velocity distribution and subsequently revise the relevant parameters in the slipstream theory.

Using the VPM to calculate the typical states of the rotor (Parameters are shown in Table 2) during the tilt transition phase of the eVTOL, the results are presented in Figure 16. The velocity distribution of the symmetrical section of the rotor is shown in Figure 17.

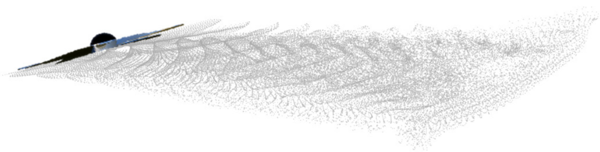

Figure 16: Wake geometries ($\alpha_s = -15°, \mu = 0.19$)

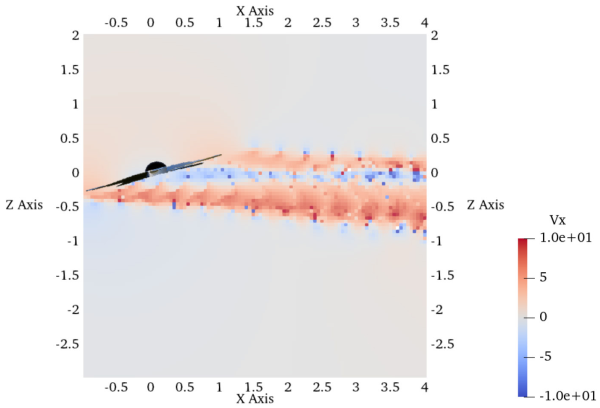

Figure 17: Side view of VPM velocity contours ($\alpha_s = -15°, \mu = 0.19$)

Usually, the rotor does not cling closely to the wing, and the distance between them falls within the range of zone of contraction and the ZFE. This paper assumes that the interference velocity of the rotor on the wing still satisfies the velocity distribution of the slipstream theory, as represented by Equation (1)-(4).

Therefore, the VPM can be used to pre-calculate the aerodynamic interference velocity of the rotor on the wing under specific conditions. Generally, there is a difference between the velocity distributions calculated by VPM and those derived from slipstream theory. First, the lift force of the wing is calculated based on the velocity field obtained from VPM. Then, using the lift force of the wing as the target value, the velocity distribution obtained from slipstream theory is holistically adjusted.

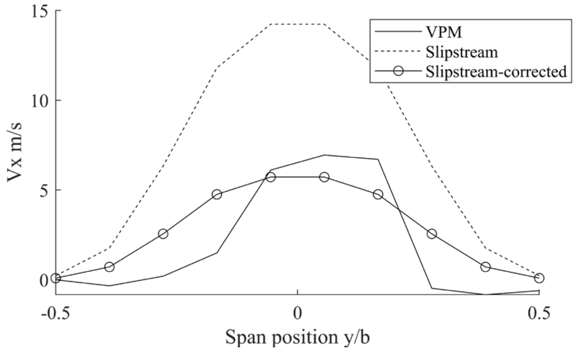

Figure 18: The velocity at the control points

Assuming that there a series of control points aligned along the Y-axis represent a straight wing, with the X-Z coordinates of these points being (1, -0.5). Figure 18 presents an example of such a correction.

Finally, correction coefficients are calculated for several state points during the tilt transition phase, and interpolation can be used to calculate the correction coefficients during the simulation process. The VPM calculations only encompass the rotor blades. Therefore, altering the configuration of the eVTOL without adjusting the rotor parameters does not necessitate a recalculation of the rotor flow field using VPM.

5. MODELLING AND SIMULATION

5.1. Aircraft Modelling Method

In this paper, a model of a vectored thrust eVTOL aircraft is established using the modelling methodology above, taking into account aerodynamic interference. The design parameters of the model are shown in Table 1 and the aircraft configuration is shown in Figure 19.

Table 1: Parameters of Aircraft

Parameters	Value
Take-off Weight (TOW)	2000 kg
Cruise Speed	80 m/s
Minimum Forward-Flight Speed (Fixed Wing)	50m/s

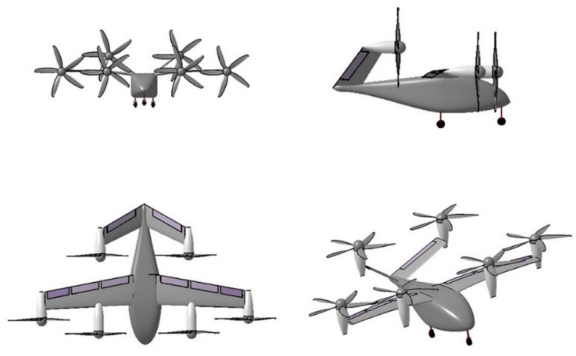

Figure 19: Schematic diagram of Aircraft

Each rotor is made up of five-blade propeller with a rigid hub, which allows pitch and rotation speed variation during flight. The shape of the propeller is based on the ATB propeller, with the same twist and airfoil distribution and an increased solidity. The specific parameters are shown in Table 2.

Table 2: Parameters of Propellers

Parameters	Value
Radius	1.5 m
Number of Blades	5
Solidity	0.2417
Blade Tip Speed	120-180 m/s
Airfoil	V43030/VR7/VR8

Taking into consideration that the propeller contains a rigid hub and an electrical propeller pitch control mechanism, no flapping, lagging and pitching hinges are set during modelling. As for aerodynamic modelling, each propeller is divided into 18 units.

A low aspect ratio straight wing is adopted, with airfoil of NACA64A223, maximum lift coefficient of 1.75, stall AOA of about 16°, and ailerons. The parameters are shown in Table 3. Each side of the wing is divided into 20 vortex lattices, with 2 rows along chord direction, and the second row includes the vortex lattices where the ailerons are located.

Table 3: Parameters of Wings

Parameters	Value
Airfoil	NACA64A223
Wingspan	8 m
Root Chord	1.36 m
Taper Ratio	0.57
Sweep Angle	-4 deg
Incidence Angle	8 deg
Aileron Relative Position	60%-90% Half-Wingspan
Aileron Relative Chord	30%
Aileron Maximum Angle	±15 deg

A V-shaped tail wing is adopted, with a symmetrical airfoil of NACA64A15, maximum lift coefficient of 1.4, and stall AOA of about 16°. The parameters of the tail wing are shown in Table 4. Each side of the tail wing is divided into 20 vortex lattices, which are divided into 2 rows along the chord direction, and the 2nd row includes the vortex lattices where the elevator is located.

Table 4: Parameters of Tail Wings

Parameters	Value
Airfoil	NACA64A15
Average Chord	0.9 m
Taper Ratio	0.82
Sweep Angle	-21.8 deg
Dihedral Angle	38 deg
Elevator Relative Position	20%-80% Half-Wingspan
Elevator Relative Chord	30%
Elevator Maximum Angle	±15 deg

The ROBIN (Ref. 32) fuselage is adopted.

The aerodynamic interference of all rotors to the wing and tail wing is considered, as well as the aerodynamic interference of the two inner-front rotors to the two rear rotors.

The separate dynamics models of each eVTOL component are stitched together to obtain the flight dynamic model of the whole aircraft. The mathematical model of the whole aircraft can be written in the form of ODE. The 4th order Runge-Kutta method is used for the solution and the time step is fixed at 5ms.

There exist three typical flight states for vectored thrust eVTOL: multi-rotor phase, fixed-wing phase, and tilt transition phase. In this paper, the speed/altitude/heading hold is designed for multi-rotor phase and fixed-wing phase respectively. The control input in tilt transition phase is obtained from the combination of control input of the first two phases according to the designed linear distribution mode (Ref. 16). The tilt angles of the six rotors are kept the same during the tilt transition phase. Control codes are burned into the flight control system for hardware-in-the-loop simulation.

5.2. Hardware-in-the-Loop Simulation Validation

In this paper, the validity of the dynamic model is verified by a hardware-in-the-loop simulation platform. The platform includes a simulation computer, a rendering computer, a flight control system, a ground measurement and control system, etc. The system architecture is shown in Figure 20. The processor of the simulation computer is an Intel Core 12900k with a processor frequency of 5.2 GHz, and the processor of the flight control system has a frequency of 200 MHz, with the control cycle of 20ms, which receives sensor data passively. The platform used in this paper is a product of Zhuhai Lonhua Helicopters Technology Co., Ltd.

The requirements of the flight control system in real-time means that the simulation computer needs to complete the control command reception, 20ms simulation calculation (time-marching 4 times), and sensor data sending in one control cycle (20ms).

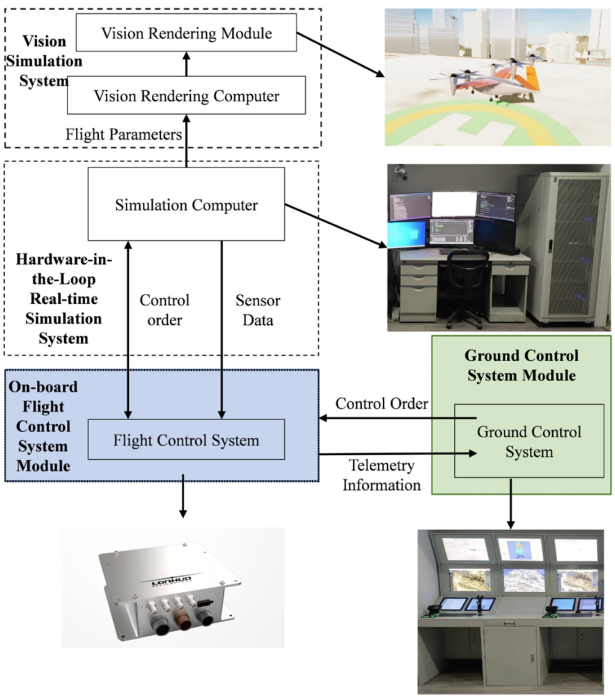

Figure 20: Schematic Diagram of Hardware-in-the-Loop Simulation Platform

A hardware-in-the-loop simulation platform is used for dynamic simulation of aircraft take-off, climb, tilt, cruise and landing. The time-domain data of a typical flight process is shown in Figure 21.

The aircraft has small fluctuations in pitch angle and control input during the tilt transition phase. The absolute value of the pitch rate does not exceed 5°/s at most. The tilt transition can be thus completed smoothly. The fluctuation of pitch angle at about 30s and 180s is due to the simple design of the controller's control law for the tilt transition phase, which does not smoothly realize the transition from the tilt transition phase to the fixed-wing phase and the reverse process.

After tilt transition phase, the aircraft continues to accelerate to the cruise speed of 80m/s during the fixed-wing phase. During this process, the attitude of the aircraft changes smoothly. It can be shown that as the forward speed increases, the pitch angle of the aircraft decreases to below 0°. This is due to a larger incidence angle is adopted for the wing to ensure that the tilt transition can be completed at a lower speed. Subsequently, the eVTOL began to decelerate gradually, and the tilt angle of the rotor nacelle increased gradually. Finally, the eVTOL completed the entire flight process.

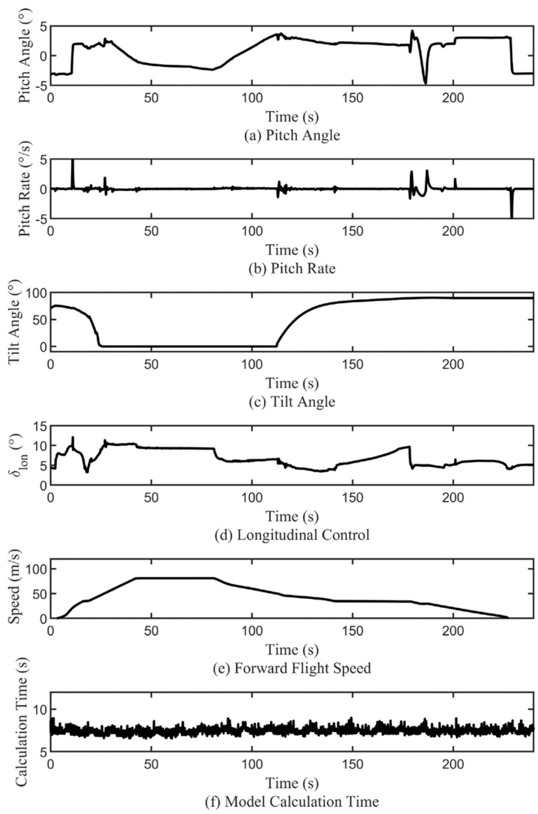

Figure 21: Results of Flight Dynamic Simulations

The model calculation time for each cycle is 7.3±0.3ms, with a maximum of 10ms. the communication delay between the simulation computer and the flight control system is 3.4±0.8ms. The sum is less than 20ms. in addition, the data log of the flight control system shows that a new sensor packet is received for each cycle, which demonstrates that the model meets the real-time requirements of the flight control system.

Table 5 shows the time consumption for each part of the model calculation. The rotor aerodynamic computation includes rotor dynamic inflow and aerodynamic computation of each blade element. Aerodynamic interference refers to computation of the velocity of the downstream control point. Vortex lattice induced velocity refers to the induced velocity of each control point required in the calculation of VLM. The model solution includes the aerodynamic computation of VLM of the wing component as well as the grouping and computation of the aircraft model. And the other includes the loss caused by data logging, program loss caused by scheduling, etc., obtained by subtracting the total time from the time of the other parts. From the table, it can be seen that the time consumption of aerodynamic interference is relatively short, which indicates that the aerodynamic interference model established in this paper has less computation consumption and is capable of real-time simulation.

Table 5: Time Consumption of Model

Computation Part	Time Consumption
Rotor Aerodynamic Computation	0.75±0.06ms
Aerodynamic Interference	0.73±0.28ms
Vortex Lattice Induced Velocity	0.41±0.27ms
Model Solution	5.09±0.43ms
Others	0.3±0.34ms
Total	7.3±0.3ms

5.3. Influence Analysis of Aerodynamic Interference

First of all, the influence of aerodynamic interference in the case of disturbance during steady-state forward flight is considered. At the forward speed of 55m/s, the following control input is executed: 1. disconnect the flight control system, all control input kept constant; 2. elevators 3° downwards for 0.5s; 3. elevators restored for 0.5s; 4. the flight control system re-accessed, and all control input is given by the control system again. The aerodynamic interference in this case can be roughly divided into three parts: propeller-wing, propeller-tail, and propeller-propeller. Figure 22 shows the influence of each part, in which the control is applied at 3s and the flight control system re-accessed at 4s, indicating that

1) The dynamic response curve with propeller-tail aerodynamic interference is basically consistent with that without. This is because the projected overlap area of each propeller and the V-tail is relatively small during the forward flight phase, causing weaker aerodynamic interference.

(2) Taking into consideration propeller-wing aerodynamic interference, the amplitude of the pitch angle increases by 20%, the time for the pitch angle to reach the peak increasing by 3%. The case considering propeller-propeller aerodynamic interference is similar to the former.

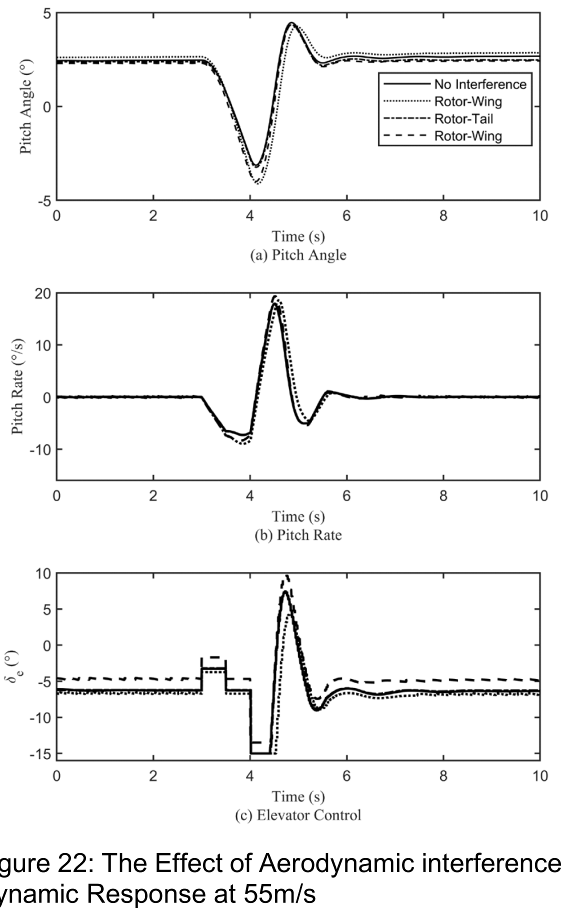

Figure 22: The Effect of Aerodynamic interference on Dynamic Response at 55m/s

The propeller wake increases the free stream velocity of the wing and increases the slope of the wing's lift-curve. Considering that the wing is in front of the center of mass of the aircraft, the increase in the slope of the wing lift-curve reduces the longitudinal stability derivatives.

The wake from the front propeller to the rear propeller reduces thrust coefficient of the rear propeller. During fixed-wing phase, tractor force increases with the increase of aircraft AOA with rear propeller pitch unchanged. Since the rear propeller is above the center of mass of the aircraft, its moment on the aircraft after disturbance is a restoring moment. Considering the aerodynamic interference similarly reduces the longitudinal stability.

The reduction of the stability derivatives decreases the frequency and damping of the short-period modes. As a result, the pitch angle amplitude is larger and the period is longer for the longitudinal disturbance of the aircraft.

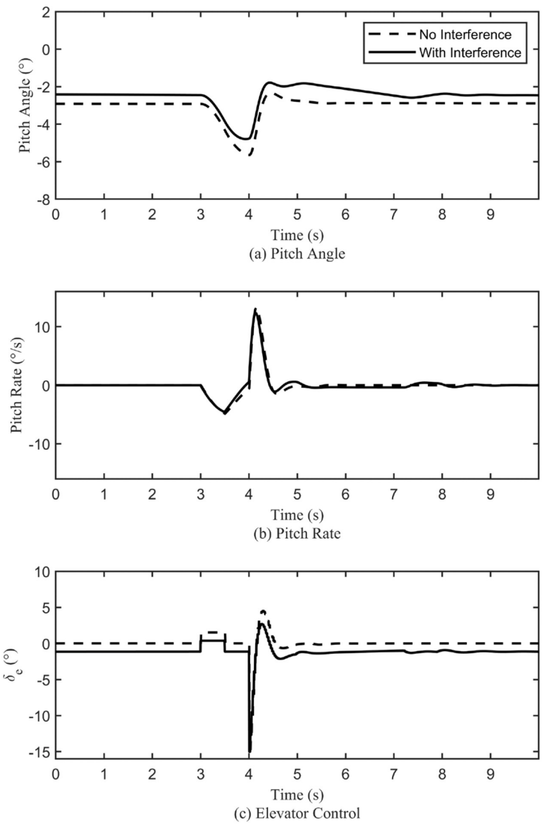

Figure 23: The Effect of Aerodynamic interference on Dynamic Response at 80m/s

Secondly, the case of steady-state forward flight at the speed of 80m/s is calculated, with the same control input and amplitude adjusted to 1.5°. The results are shown in Figure 23. It can be seen that aerodynamic interference affects the pitch angle and control input of the trim state but has less effect on angular rate change. This is due to the ratio of aerodynamic interference to the free stream velocity lower at high speed, in other words, the effect of aerodynamic interference on dynamic response less obvious at higher speed.

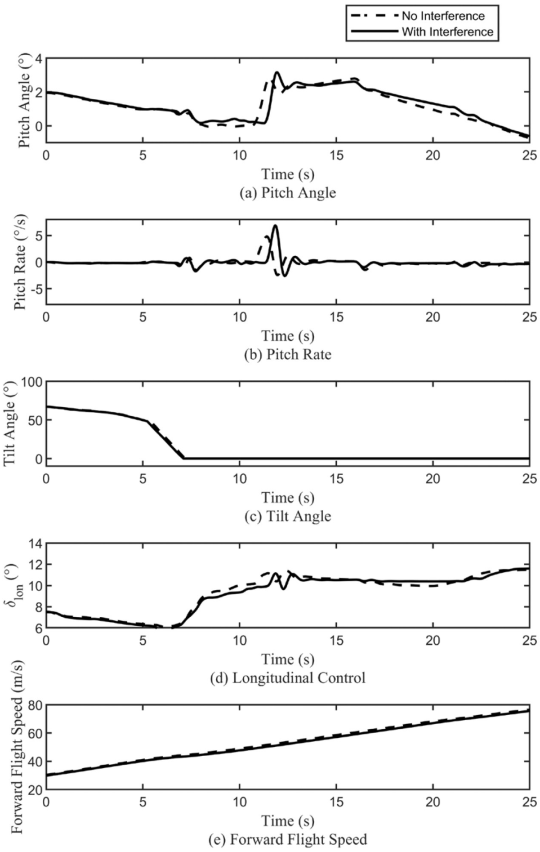

Figure 24: The Effect of Aerodynamic interference during Tilt Transition Phase

Next, the influence of aerodynamic interference in the case of tilt transition phase is calculated. The same control law and initial condition are adopted to simulate the model with/without aerodynamic interference. The difference is shown in Figure 24. It can be seen that the aerodynamic interference has less influence on pitch and longitudinal control input during the tilt transition phase at forward speed of 30m/s to 50m/s. This may be because when the nacelle tilt angle is large, the distance between the rotor and the wing in the Z direction is far enough, so the influence of the rotor on the wing is relatively small. At about 7s, the pitch angle of the aircraft has a slight fluctuation, but the aerodynamic interference has a small effect on amplitude and phase of this fluctuation. At about 12s, the control mode is changed from tilt transition mode to fixed-wing mode. Mode switching of the controller leads to oscillations in pitch angle. Compared to the model without aerodynamic interference, there exist a phase lag and an about 30% increase in peak of that with interference, since aerodynamic interference reduces the frequency and damping of the longitudinal short period of the aircraft.

6. CONCLUSIONS

Aiming at the characteristics of vectored thrust eVTOL with diverse configurations and complex aerodynamic interference, this paper proposes a real-time simulation method of flight dynamics. Through the aircraft dynamics modelling and hardware-in-the-loop simulation verification of vectored thrust eVTOL, the following conclusions can be obtained:

1. Models for the components of eVTOL have been developed and validated. These models can be utilized to establish various configurations of eVTOL.
2. The real-time flight dynamic simulation model of vectored thrust eVTOL established by the method of this paper can be used for the whole process dynamic simulation of take-off, climb, tilt transition, cruise, and landing. The real-time requirements of the flight control system can be satisfied. And it can be applied to the control law design and verification of the flight control system for the whole flight process.
3. The aerodynamic interference model proposed in this paper can be used for real-time simulation. This model is capable of accurately calculating the aerodynamic interference of propeller-wing and propeller-propeller, and it can also be corrected based on VPM to compute the aerodynamic interference of rotor-wing.
4. The aerodynamic interference model has an effect on the dynamic response of the aircraft at the end of the tilt transition phase and fixed-wing phase at low speed. The longitudinal stability derivatives of the model decrease and pitch rate peak increases when considering aerodynamic interference.

Author contact:

Liangjun Li	liliangjun2006@126.com
Fan Sun	sunfan2021314@163.com
Yiran Gong	yrgong@outlook.com
Tianheng Yao	yth21@mails.tsinghua.edu.cn
Wei Zhang	13411375087@163.com
Chen Jiang*	jc2017@mail.tsinghua.edu.cn
Haowen Wang	bobwang@tsinghua.edu.cn

7. REFERENCES

1. Rajendran S., Srinivas S., “Air taxi service for urban mobility: A critical review of recent developments, future challenges, and opportunities,” *Transportation research part E: logistics and transportation review*, Vol.143, Nov. 2020, 102090. DOI: 10.1016/j.tre.2020.102090.
2. Doo J. T., Pavel M. D., Didey A., Hange C., Diller N. P., Tsairides M. A., Smith M., Bennet E., Bromfield M., Mooberry J., “NASA Electric Vertical Takeoff and Landing (eVTOL) Aircraft Technology for Public Services–A White Paper,” NASA Document Number 20205000636, 2021.
3. Electric VTOL News™ by the Vertical Flight Society, “eVTOL Aircraft Directory,” 2023, https://evtol.news/aircraft.
4. Kiesewetter L., Shakib K. H., Singh P., Rahman M., Khandelwal B., Kumar S., Shah K., “A holistic review of the current state of research on aircraft design concepts and consideration for advanced air mobility applications,” *Progress in Aerospace Sciences*, Vol. 142, Oct. 2023, 100949. DOI: 10.1016/j.paerosci.2023.100949.
5. Zahn D., Naru R., Guion A., Eggum S., “UAM Instrument Flight Procedure Design and Evaluation in the Joby Flight Simulator,” NASA AAM-NC-115-001, 2023.
6. Sun J., Li B., Wen C., Chen C., “Design and implementation of a real-time hardware-in-the-loop testing platform for a dual-rotor tail-sitter unmanned aerial vehicle,” *Mechatronics*, Vol. 56, Dec. 2018, pp. 1-15. DOI: 10.1016/j.mechatronics.2018.10.001.
7. Sridharan A., Rubenstein G., Michael Moy D., Chopra I., “A Python-Based Framework for Computationally Efficient Trim and Real-Time Simulation Using Comprehensive Analysis,” *Journal of the American Helicopter Society*, Vol. 63, (1), Jan. 2018, pp. 1-15. DOI: 10.4050/JAHS.63.012003.
8. Padthe A., Sridharan A., Berger T., Lopez M., Glover E., “Framework for Real-Time Closed-Loop Simulation of Advanced Rotorcraft Configurations Using Comprehensive Flight Dynamics Models,” Vertical Flight Society 80th Annual Forum, Montreal, Quebec, Canada, May 2024.
9. Cook J., “A strip theory approach to dynamic modeling of evtol aircraft,” AIAA 2021-1720, AIAA SciTech 2021 Forum, Virtual Event, Jan. 2021.
10. Simmons B. M., Murphy P. C., “Aero-propulsive modeling for tilt-wing, distributed propulsion aircraft using wind tunnel data,” *Journal of Aircraft*,

Vol. 59, (5), Sept. 2022, pp. 1162-1178. DOI: 10.2514/1.C036351.

11. Gladfelter M., He C., Saberi H., Malpica C., Johnson W., Silva C., “Enhanced Flight Dynamics Models with Aerodynamic Interference for Real-Time Simulation of VTOL Concept Vehicles,” Paper VFS 2023: 18113-18135, Vertical Flight Society 79th Annual Forum, Alexandria, May 2023.
12. Prabhakar N., Salucci F., Karbowski D., “Estimating Mission-Based Energy and System Dynamics of e-VTOL Aircraft,” Paper AIAA, 2023: 3922-3934, AIAA AVIATION 2023 Forum, San Diego, CA and Online, June 2023.
13. Veble M. G., Bain J., Bevirt J., Stoll A., “A CFD Based Method to Model Aerodynamic Interactions in Complex eVTOL Configurations for Realtime and Medium Fidelity Simulation,” Paper VFS 2021: 16786-16793, Vertical Flight Society 77th Annual Forum, Alexandria, May 2021.
14. Stoll A., Mikic G., “Transition performance of tilt propeller aircraft,” Paper VFS 2022: 17443-17459, Vertical Flight Society 78th Annual Forum, Fort Worth, Texas, May 2022.
15. Wang H., Sun W., Zhao C., Zhang S., Han J., “Dynamic modeling and control for tilt-rotor UAV based on 3D flow field transient CFD,” *Drones*, Vol. 6, (11), Nov. 2022, pp. 338. DOI: 10.3390/drones6110338.
16. Sun F., “Multi-rotor Tiltable eVTOL Flight Dynamics modeling and Real-Time Simulation,” Beijing: Tsinghua University, 2023: pp. 66-80(in Chinese).
17. Tan J., Wang H., “Simulating unsteady aerodynamics of helicopter rotor with panel/viscous vortex particle method,” *Aerospace Science and Technology*, Vol. 30, (1), Oct. 2013, pp. 255-268. DOI: 10.1016/j.ast.2013.08.010.
18. Katz J, Plotkin A., *Low-speed aerodynamics*, Cambridge University Press, New York, NY, 2001, pp. 340-350.
19. Harris F. D., “Hover performance of isolated proprotors and propellers-experimental data,” NASA/CR-2017-219486, 2017.
20. Deters R. W., *Performance and slipstream characteristics of small-scale propellers at low Reynolds numbers*, University of Illinois at Urbana-Champaign, Champaign-Urbana, 2014, Chapter 6.
21. Ghee T. A., Berry J. D., Zori L. J., Elliott J. W., “Wake geometry measurements and analytical calculations on a small-scale rotor model,” NASA TP-3584, ATCOM TR-96-A-007, 1996.
22. Arthur E. P., Berry D. B., “Description of the US Army small-scale 2-meter rotor test system,” NASA TM-87762, 1987.
23. Weber J., Brebner G., Kuchemann D., “Low-Speed Tests on 45-deg Swept-Back Wings Parts I and II, Part I: Pressure Measurements on Wings of Aspect Ratio 5,” Her Majesty’s Stationery Office (HMSO), Reports and Memoranda No.2882, 1951.
24. Xia Z., Yang Y., “Unsteady numerical simulation of interaction effects of propeller and wing,” *Acta Aeronautica et Astronautica Sinica*, Vol. 32, (7), 2011, pp. 1195-1201(in Chinese). DOI: CNKI:11-1929/V.20110316.1332.003.
25. Khan W., Nahon M., “Development and validation of a propeller slipstream model for unmanned aerial vehicles,” *Journal of Aircraft*, Vol. 52, (6), Nov. 2015, pp. 1985-1994. DOI: 10.2514/1.C033118.
26. Goates J. T., “Development of an Improved Low-Order Model for Propeller-Wing Interactions,” Utah State University, Logan, Utah, 2018. Chapter 3.
27. Stone R. H., “Aerodynamic modeling of the wing-propeller interaction for a tail-sitter unmanned air vehicle,” *Journal of Aircraft*, Vol.45, (1), Jan. 2008, pp. 198-210. DOI: 10.2514/1.15705.
28. Dong Z., *Jet Flow Mechanics*, Science Press, Beijing, 2005, pp. 88-95 (in Chinese).
29. Khan W., Nahon M., “Development and validation of a propeller slipstream model for unmanned aerial vehicles,” *Journal of Aircraft*, Vol. 52, (6), Nov. 2015, pp. 1985-1994. DOI: 10.2514/1.C033118.
30. Veldhuis L. L. M., *Propeller wing aerodynamic interference*, Delft University of Technology, Delft, 2005, Chapter 5.
31. Stokkermans T. C. A., Usai D., Sinnige T., Veldhuis L. L. M., “Aerodynamic interaction effects between propellers in typical eVTOL vehicle configurations,” *Journal of Aircraft*, Vol. 58, (4), July 2021, pp. 815-833. DOI: 10.2514/1.C035814.
32. Freeman C. E., Mineck R. E., “Fuselage surface pressure measurements of a helicopter wind-tunnel model with a 3.15-meter diameter single rotor,” NASA-TM-80051, 1979.